THE ASTROPHYSICAL JOURNAL, 453:284–292, 1995 November 1

X-RAY EMISSION FROM THE SUPERNOVA REMNANT CTA 1

F. D. SEWARD, B. SCHMIDT, AND P. SLANE
Harvard-Smithsonian Center for Astrophysics, 60 Garden Street, Cambridge, MA 02138
Received 1994 October 11; accepted 1995 May 10

ABSTRACT

Three pointings of the *ROSAT* PSPC have been used to map the X-ray emission of CTA 1. Emission is brightest at the center and extends in all directions to the boundaries of the remnant. The luminosity is model-dependent and (at 1.4 kpc), is, $L_x(0.1\text{–}2.4\ \text{keV}) = 5\text{–}8 \times 10^{34}$ ergs s^{-1}. Emission from the center is harder and considerably brighter than that from the rim. Spectra from several parts of the remnant are fitted with two component models. Both a two-temperature thermal model and a model consisting of a power law and a soft thermal component produce good fits to all regions. The spectra do not allow us to distinguish between a remnant with hot evaporated material at the center, or an old Crab-like remnant. Both are plausible models for CTA 1.

The *ROSAT* HRI was used to obtain an accurate location of a bright unresolved source within the remnant. This is identified as a background active galactic nucleus. Properties of eight weaker, unresolved X-ray sources within or nearby the remnant are tabulated

Subject headings: galaxies: Seyfert — ISM: individual (CTA 1) — supernova remnants — X-rays: ISM

1. INTRODUCTION

There are currently 11 supernova remnants (SNRs) which contain or are associated with young neutron stars, pulsars positively identified by detection of radio or X-ray periodicity (Seward 1989; Caraveo 1993). These associations are important because they not only show that the remnant originated in gravitational collapse of a massive star but also give an age for the pulsar and remnant. Another 10 remnants show central X-ray emission, perhaps due to deposition of energy by a pulsar, but perhaps not. Interpretation of observations is not straightforward because characteristics of both SNR shells and neutron-star central energy sources vary widely. Emission from a central source can dominate, as in the Crab Nebula, or can be almost hidden by other emission, as in RCW 103.

The search for pulsars is expected to become more difficult in older remnants because the power radiated by the neutron star will gradually decrease with time. High-velocity neutron stars can even drift from within the remnant. Properties of remnants containing, or likely to contain, neutron stars are given in reviews by Weiler (1985), Seward & Wang (1988), and by Seward (1989). Properties of pulsars which are found to emit X-rays have been reviewed by Ogelman (1994).

There is a class of remnants, of which CTA 1 is a member, characterized by radio shells and by diffuse X-ray emission that has maximum brightness in the interior (Long et al. 1991); one of these (W44) is shown to emit mostly thermal X-rays (Rho et al. 1994). Early observations of CTA 1 revealed diffuse X-rays and a moderately bright unresolved source in the interior (Seward 1990). CTA 1 is a large-diameter, probably old, remnant with low surface brightness. It was an ideal target for the *ROSAT* PSPC. Our observations reveal that the bright unresolved interior source is a background active galaxy (AGN) and not physically associated with CTA 1. The morphology and spectrum of the diffuse emission, however, suggests a nonthermal origin. Other faint unresolved sources are also found within the shell and might be candidates for a pulsar. The *ROSAT* data indicate that CTA 1 has the appearance of an older Crab-like remnant.

The radio characteristics of CTA 1 are given by Sieber, Salter, & Mayer (1981) and by Pineault et al. (1993). The radio diameter is 107′, and the shell is bright in the south and in the east but fades to near invisibility in the north and northwest. There is a faint bar of radio emission extending north–south across the face of the remnant. We reproduce contours from the 1720 Hz map of Sieber et al. in Figure 2. The optical morphology is discussed by Fesen et al. (1981). Diffuse O [III] and S [II] are observed associated with the radio-bright parts of the shell. The general appearance and radio spectrum produce a convincing identification as a SNR. Pineault et al. also map H I in the vicinity and identify a bar of emission in the north which they propose to be a shell of neutral hydrogen swept up by the shock. This defines a northern boundary for the remnant and the observed velocity of the neutral hydrogen allows them to derive a kinematic distance of 1.4 ± 0.3 kpc.

Sieber et al. (1981) summarize distance estimates based on the Σ–D relationship which fall in the range 1–2 kpc. They estimate an age of 1×10^4 yr, an ISM density of 0.04 cm^{-3} and an explosion energy of 1×10^{51} ergs. On the other hand, Pineault et al. use an ISM density of 1 cm^{-3} to estimate the mass of the swept-up hydrogen shell.

In the X-ray band, CTA 1 and the background AGN (source 2 in Table 4 and Fig. 3) were first detected by *Uhuru* and have been observed by several X-ray missions since. Table 1 summarizes the results. Count rates have been normalized to the rate of the Crab Nebula (which was also observed with these same detectors). There is more variation than there should be. Detectors sensitive over the same energy band should give the same relative rate and this is not so in Table 1. The most likely source of error is in background estimation. It seems unlikely that the AGN would vary enough to explain these rates. The *ROSAT* results, however, do indicate that the *Einstein* IPC rate given here is too low.

2. *ROSAT* OBSERVATIONS

Three nominal 10 ks observations with the PSPC were used to map the diffuse emission. One pointing was at the approx-

TABLE 1

OBSERVATIONS OF CTA 1

Instrument	Energy Range (keV)	Count Rate (millicrab)	Reference
Uhuru	2–6	1.74 ± 0.42	Forman et al. 1978
Ariel V	2–10	1.14 ± 0.20	McHardy et al. 1981
HEAO-1 A1	1–20	1.31 ± 0.17	Wood et al. 1984
Einstein IPC	0.2–4	1.10 ± 0.22	Seward 1990
Einstein MPC	1.5–10	0.54 ± 0.11	Seward 1990
EXOSAT ME	1–20	0.54 ± 0.05	HEASRC data base
ROSAT PSPC	0.1–2.4	3.6 ± 0.3	This paper

imate center of CTA 1, another was just inside the eastern rim, and the third, just inside the southern rim. All were accomplished in 3 days. The HRI observation of 1E 0000+726, although short, was done in two segments separated by 8 months. Spacecraft and detectors are described by Aschenbach (1988). Observations are summarized in Table 2.

3. MORPHOLOGY

Figure 1 shows our X-ray picture of CTA 1. To generate this map, the three PSPC observations were combined. Each field was first "cleaned" by removing data from short intervals where the count rate was observed to increase significantly from the average. This interval generally was of duration $\approx$300 s and at the end or beginning of each acquisition. The exposures were consequently shortened to 75%–82% of the time listed in Table 1. Data were restricted to the energy band 0.5–2.4 keV. The three fields were then registered and added (with considerable overlap). The corresponding exposure maps were added and the exposure set to zero when the sum was less than $\approx$1200 s to eliminate statistical artifacts. The summed data were divided by the exposure and the resultant array smoothed with a Gaussian function.

To show faint diffuse emission, a smoothing function with FWHM of 7′ was used. These data are shown in Figure 1 and as contours in Figure 3. The X-ray remnant is egg-shaped with size 80′ × 100′. There is a faint feature extending $\approx$20′ to the west. The two brightest unresolved sources (4 and 9 in Fig. 3) have been subtracted from the data of Figure 1. They have not been subtracted from Figure 2 which shows the X-ray contours overlaid on a radio map. The X-ray boundary in the south and in the east coincides with the radio shell. In the north, the X-ray boundary is close to the H I shell of Pineault et al. (1993). The faint western arm also coincides with a radio feature which can be seen clearly in Figure 2 in their paper. Thus CTA 1 is clearly a remnant characterized by a partial radio shell and X-ray emission from the center. There may be X-ray emission from the shell in the north and in the east. There is evidence for the expected soft thermal emission in the spectrum.

The appearance of unresolved sources in the PSPC depends on the distance from the center of the field. Sources more than 20′ from the center are considerably broadened and, if not bright, difficult to see. Figure 3 shows unresolved sources within the boundary of CTA 1. Data from the field centers were added and smoothed using a Gaussian of 0.′6 FWHM. Eight unresolved sources are clearly seen and the position of the bright source just outside the remnant is indicated. Note that several of the sources are encompassed by a swelling of the nearest surface brightness contour. We suspect that some of the structure of these contours is not significant with respect to the remnant.

The total PSPC counting rate from CTA 1 was 3.5 ± 0.3 counts s^{-1}. This was calculated by measuring the rate from the bright central region in one PSPC field and then using this to normalize the rate of the remnant in the combined image.

4. SPECTRAL STUDIES

Four sections of the remnant were selected for spectral fitting: a circular region of radius 10′ containing the bright center; an annulus of inner and outer radii 10′ and 20′ surrounding this; a rectangular box of dimension 32′ north–south and 22′ east–west, containing the bright ridge south of the center; and a rectangular box of dimension 52′ north–south and 20′ east–west just inside the east limb. Data and background for each region were obtained from a single *ROSAT* observation. Backgrounds in each case were taken from the same field but outside the remnant. The bright AGN was excluded.

We seek a plausible model that produces acceptable fits to all four regions. We first note that there are no events below 0.4 keV in any of the pulse-height spectra. Absorption in the ISM has removed all photons from the "$\frac{1}{4}$ keV" band. The column density, N_H, is therefore greater than $\approx 1 \times 10^{21}$ atoms cm^{-2}. Furthermore, the total galactic column density in this direction is 2.5×10^{21} or $\log N_H = 21.4$ (Starke et al. 1992), which we will take as the maximum acceptable column density for spectral fits. It is also obvious, looking at the pulse height spectra, that emission from the center is harder than emission from the limb.

Table 3 summarizes results of spectral fitting using four models. We first fit a single-temperature Raymond-Smith

TABLE 2

ROSAT OBSERVATIONS OF CTA 1

Number	Instrument	Date	R.A.(2000)	Decl.(2000)	Exposure (s)
500071	HRI	1992 Jan 11 and Sep 14	$00^h02^m36^s$	72°54′.6	3145
500070	PSPC	1993 Jan 11	00 05 38	73 01.8	10517
500072	PSPC	1993 Jan 10	00 03 36	72 21.6	7108
500073	PSPC	1993 Jan 12	00 13 45	72 51.6	7015

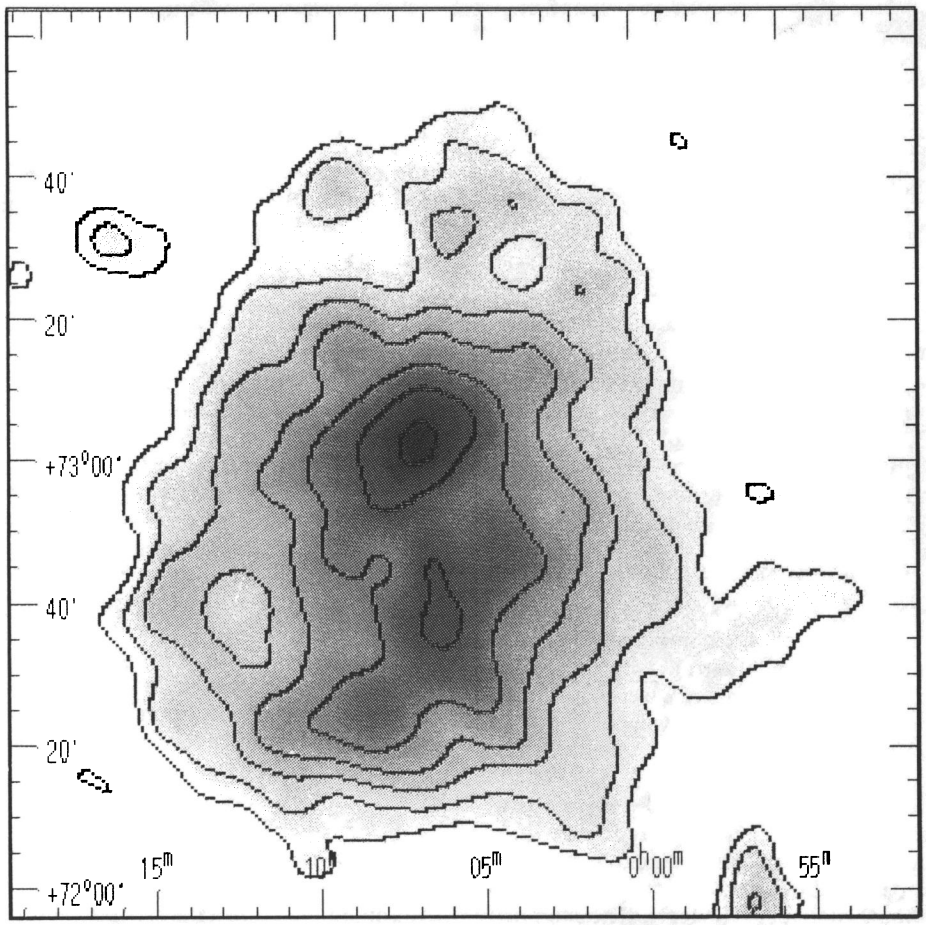

FIG. 1.—X-rays from CTA 1. Three PSPC observations are superposed in this map. Data have been smoothed over ≈7′. The two brightest unresolved sources in the field have been removed. Contours of constant X-ray surface brightness are logarithmic and spaced a factor of 1.24 apart.

model to each of the four regions, allowing temperature, T, and N_H to vary. χ^2 was high and these fits, when inspected visually, were obviously unacceptable. The best predicted spectra were too narrow to fit the data. We next fit a power-law model, varying energy index, α, and N_H. Better fits were obtained; α varied from 1.3 in the central region to 3.9 at the rim and the best-fit N_H varied from 1.1×10^{21} at the center to 2.5×10^{21} at the rim. Fits were acceptable except at the limb where the lowest reduced χ^2 was 2.1. Because of this and because the best-fit N_H varied a factor of 2 from center to edge of remnant, we progressed to two-component models.

We tried two: a two-temperature thermal model, and a thermal/power-law combination. All thermal components were Raymond models with standard cosmic abundances. In the following discussion, it is important to remember that the two-component models contain enough parameters to guarantee a good fit to the data (irrespective of the suitability of the model) and that these fits are not unique. For simplicity, we required N_H and the low and high temperature (or index) to be the same for all four regions. Acceptable fits were obtained letting only the ratio of the contribution of the two components vary from region to region. The XSPEC code was used

TABLE 3

SPECTRAL PARAMETERS FOR CTA 1

Model	Parameter	Best-Fit Values	90% Confidence Range	Reduced χ^2
Single temperature	N_H (10^{21})	0.5–2.5	...	1.8–4.3
	T (keV)	0.26–4.4	...	
Power law	N_H (10^{21})	1.1–2.5	...	0.9–2.1
	α (energy)	1.3–3.9	...	
Two temperature	N_H (10^{21})	2.3	1.0–2.5	0.9
	T_{low} (keV)	0.22	0.20–0.28	
	T_{high} (keV)	2.04	1.5–3.2	
Thermal and nonthermal	N_H (10^{21})	2.3	1.5–2.5	0.9
	T_{low} (keV)	0.23	0.21–0.29	
	α (energy)	1.9	1.3–2.1	

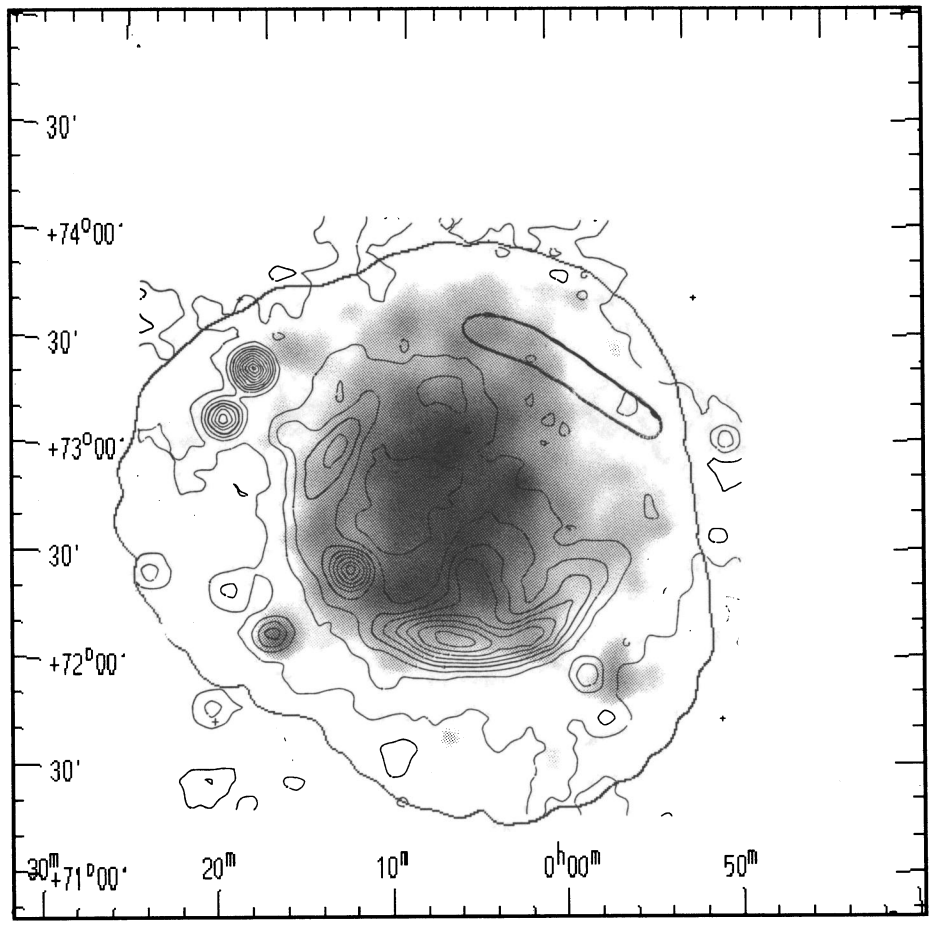

FIG. 2.—X-ray and radio emission from CTA 1. Fine contours are taken from the 1720 MHz map of Sieber et al. The X-ray features are in gray-scale with the unresolved sources 1E 0000+726 and 4C 71.01 now included. The northern radio H I shell is also represented by a heavy contour of dimension 10′ by 60′. The outer contour shows the boundary of the region observed by *ROSAT*.

to fit all four regions at the same time. Both two-component models produced fits with reduced $\chi^2 = 0.9$.

Table 3 lists the best-fit spectral parameters and the range of parameter values which can be used within 90% confidence limits. Since the parameters are coupled, all values within these ranges cannot be chosen arbitrarily. If an arbitrary value for one parameter is chosen (within the range), it is possible to find values for the other parameters (within their respective ranges) which, when used in a spectral fit, will produce a χ^2 value within the 90% confidence range. It turns out that the limb spectrum, where the soft component dominates, tends to fix the range of the soft spectral parameter, and the central spectrum, where the hard component dominates, tends to fix the high-temperature parameter.

Although not forbidden, we have no reason to believe that N_H varies appreciably over the regions used for spectral analysis. Since spectral fits are acceptable using a constant N_H, we assume this is so in the analysis.

The two-temperature model with parameters listed in Table 3 produces an acceptable spectral fit. The physical interpretation of the model is a low-temperature shell surrounding a warmer interior. The best fit occurs using a temperature of 0.22 keV for material in the shell and a temperature of 2.0 keV for interior material, leaving the ratio of the two components as the only variable.

The second model assumes that the harder radiation from the interior is nonthermal and uses a power-law spectrum to represent this. Again a low-temperature shell is assumed to surround the interior. The spectral fit produced by this model is equally good and the best-fit temperature of material in the shell is almost the same as before. We cannot distinguish between these two two-component models using *ROSAT* spectra alone.

We now estimate the properties of the remnant as a whole. No spectral analysis was done for the northern and western limbs because these regions were not at the center of any of the three PSPC fields. We assume that these parts have the same spectrum as the east limb and the ridge which are the same within uncertainties. The flux at the detector (0.1–2.4 keV) is $F_x = 4.4 \times 10^{-11}$ ergs cm^{-2} s^{-1}. Using the two-temperature/thermal-nonthermal model the luminosity, at a distance of 1.4 kpc, is $L_x = 4.7/8.2 \times 10^{34}$ ergs s^{-1}. Over the entire remnant, 17/33% of L_x is from the soft thermal component. In addition, the flux in the band 2.4–12 keV is predicted, from this model, to be $1.12/1.07 \times 10^{-11}$ ergs cm^{-2} s^{-1} or 0.48/0.46 millicrab which may be compared with past observations listed in Table 1. It is in reasonable agreement with data from the *Einstein* MPC and the *EXOSAT* ME detectors but, since both models give the same prediction, these previous observations cannot be used to distinguish between them. We note that the thermal-nonthermal model has the stronger soft component (which is strongly absorbed in the ISM) and the calculated luminosity is thus higher and, apparently, quite model-dependent.

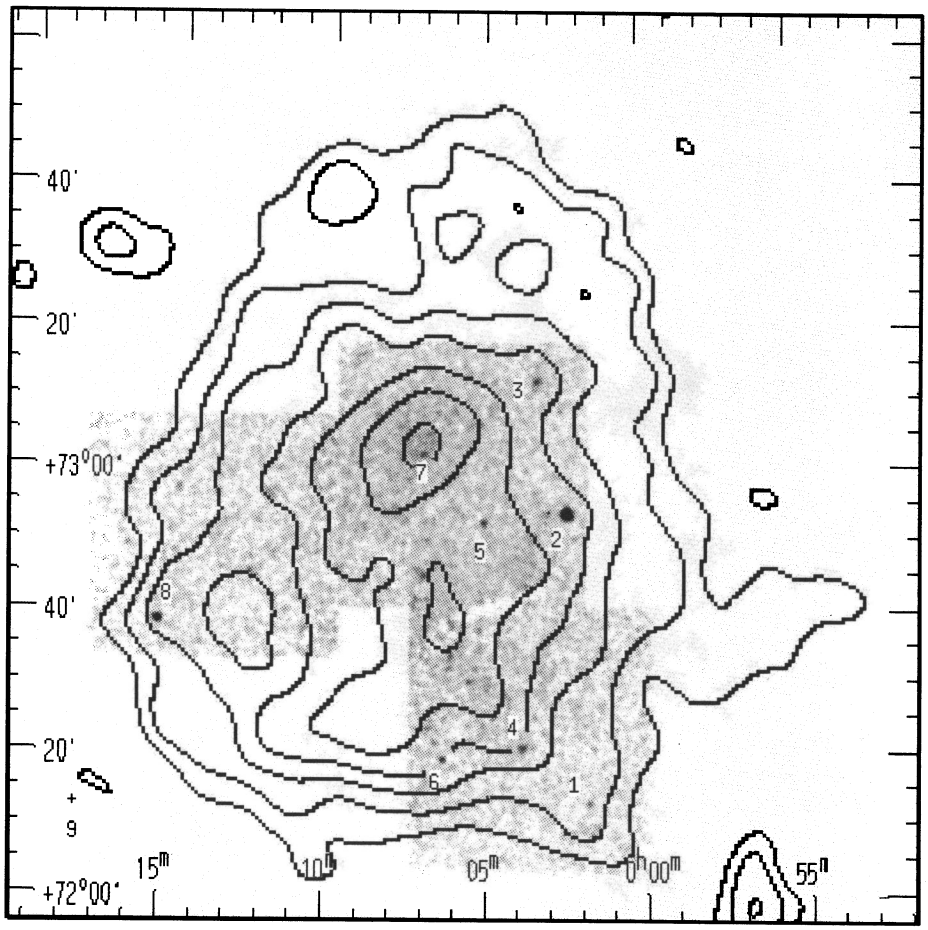

FIG. 3.—X-ray contours of Fig. 1 overlaid on a gray-scale map of X-ray emission from the field centers. Data are smoothed over 0.6 to show unresolved sources. Source numbers are the same as those in Table 4. A small strip between the center and south fields has been excluded because of low exposure due to shadowing of the window support.

5. UNRESOLVED SOURCES WITHIN CTA 1

There are nine sources in the observed region which are bright enough, and/or central enough, to be clear detections. There are at least this many more present at lesser significance. To compile a "complete" list of sources, in this area of varying background, would require great care and we did not attempt it. Positions and strengths of the nine sources, taken from the *ROSAT* standard processing (SASS), are given in Table 4. Accuracy of position in the central region of the detector is limited to $\sim 10''$ by systematics. One source, no. 9, is 43′ off axis and here the asymmetric shape and blur of the image limits accuracy to $\sim 1'$. Identifications listed in Table 4 are within these uncertainties.

TABLE 4

UNRESOLVED PSPC SOURCES WITHIN AND NEAR CTA 1

Number	R.A.(2000)	Decl.(2000)	Counts ks^{-1}	Counterpart
1.....	$0^h01^m45^s.9$	72°14′01″	3.6	K0 star? HD 224891
2.....	0 02 26.8	72 54 35	42.1	AGN, this paper
3.....	0 03 22.5	73 13 13	9.1	
4.....	0 03 51.5	72 21 41	7.9	PLMG 24?
5.....	0 05 05.7	72 53 18	5.3	
6.....	0 06 20.3	72 19 59	5.1	
7.....	0 07 02.1	73 02 59	12.9	
8.....	0 15 27.2	72 39 54	15.4	
9.....	0 17 38.6	72 12 04	18.8	4C 71.01, PLMG 59

There are 33 unresolved radio sources in the maps of Sieber et al. (1981). These are prominent radio features and one wonders if there are X-ray counterparts. Only one of these, 4C 71.01, appears in X-rays. This is probably source 9 in Table 4. Pinault et al. (1993) list 64 unresolved sources at 1420 MHz. Source 9 (again) and source 4 have possible counterparts in this list (designated PLMG in Table 4). Note that the area covered by both radio surveys is larger than the area of the combined *ROSAT* fields and that some radio sources are far off-center of the X-ray fields. A search for X-ray counterparts to the radio sources is therefore neither complete nor to uniform sensitivity.

5.1. 1E 0000+726

The location of the brightest source within CTA 1 (number 2 in Table 4 and Fig. 3) was measured with the *ROSAT* HRI as R.A. = $00^h02^m25^s.7$, decl. = 72°54′40″ (2000) with an accuracy of 4″. This is only 6″ different than, and more accurate than, the PSPC position listed in Table 4.

We obtained *B* and *R* CCD images in a 11′ × 11′ region around source 2 using the Fred Lawrence Whipple 1.2 m telescope + FORD 2048 × 2048 CCD. The images were bias-subtracted and flat-fielded and showed a blue object ($B \approx 18$ mag) within the error circle of the *ROSAT* HRI (Fig. 4). The position of this object, derived by determining the transformation for the CCD from 18 *HST* guide stars is ($00^h02^m25^s.96$ + 72°54′38″.5). A low-dispersion spectrum (15 Å) of this object

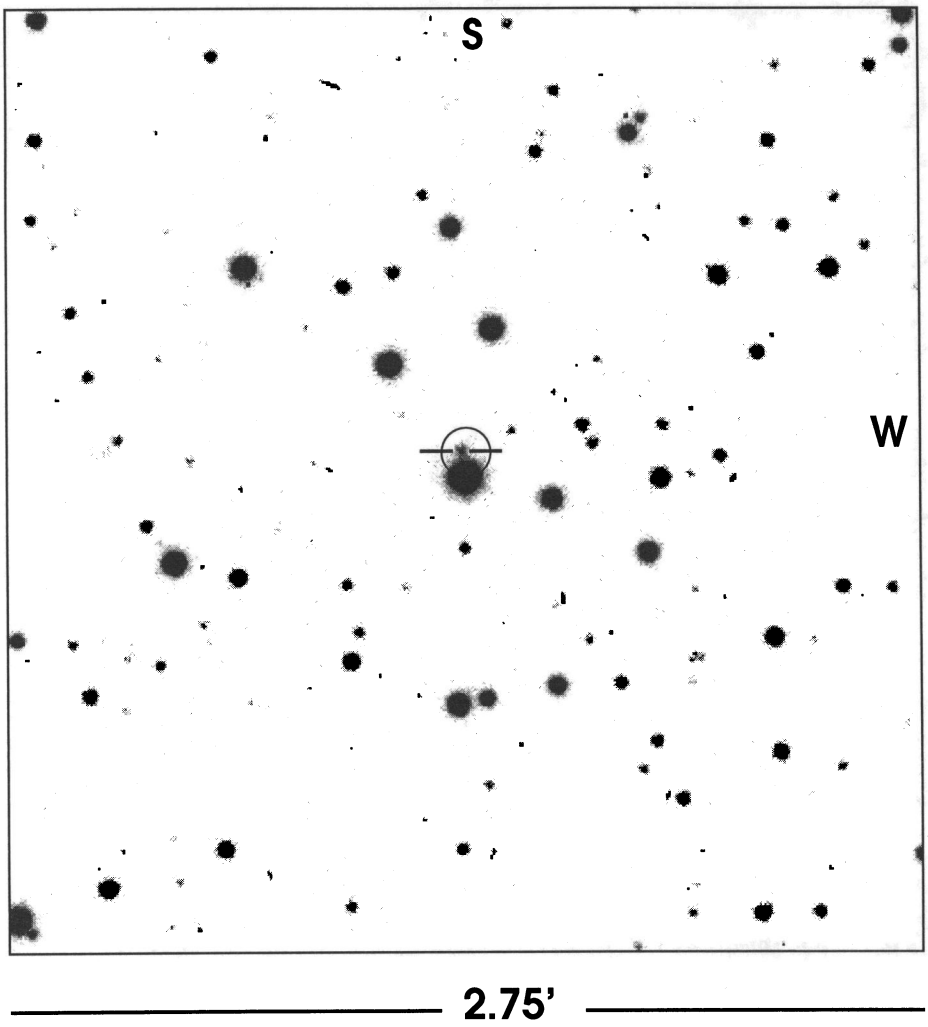

FIG. 4.—*R*-band CCD image showing the optical counterpart 1E 0000+72. The HRI error circle is 10″ in diameter.

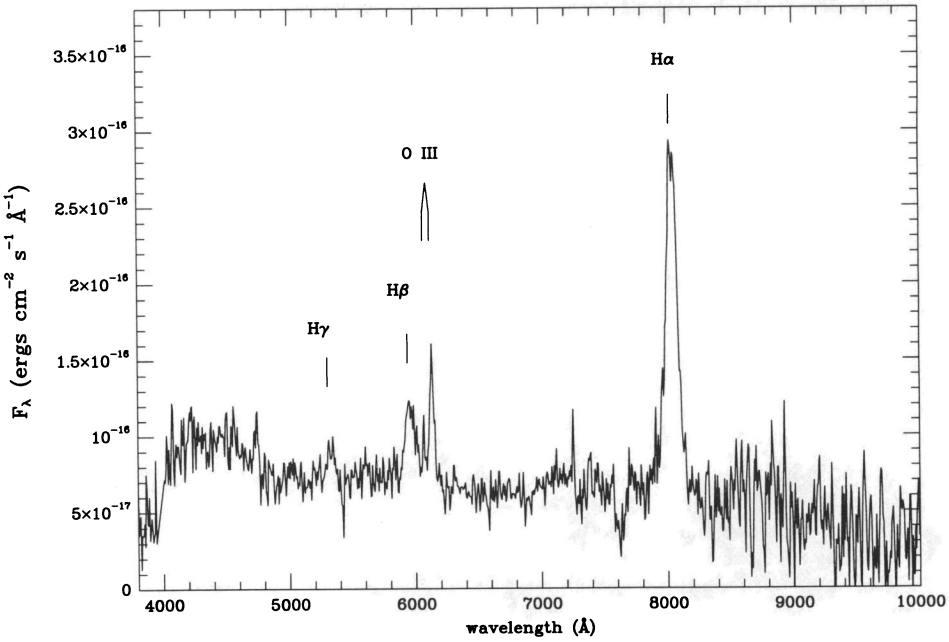

FIG. 5.—Optical spectrum of the object marked in Fig. 4. The emission lines are typical of AGNs.

TABLE 5

CHARACTERISTICS OF 1E 0000+726

Parameter	Value
V	≈ 18
z	0.225
f_x/f_{opt}	3–7
L_x (0.5–2.4 keV).....	2.3×10^{44} ergs s^{-1}
Best-fit index	1.1
Best-fit log n_H	21.4

was obtained using the Red Channel Spectrograph on the MMT. The object's spectrum shows a continuum with strong broad lines (Fig. 5) and is consistent with an AGN at a redshift of $z = 0.225$.

PSPC data were used to measure the spectrum which was assumed to be a power law. The best-fit index and absorption listed in Table 5 were used to calculate the X-ray luminosity. Although the uncertainties are very large, these numbers are as expected for an AGN in this location. The observed X-ray flux calculated is 4.7×10^{-13} ergs cm^{-2} s^{-1} and L_x(0.5–2.4 keV) = 2.3×10^{44} ergs s^{-1}, with $z = 0.225$ and $H_0 = 50$. After correcting the flux to 6.5×10^{-13} in the band 0.3–3.5 keV, the monograph of Maccacaro et al. (1988) was used to derive the ratio of X-ray to optical flux as 3 ± 2. This is well within the range expected for AGNs. All is therefore consistent with the identification of this object as an AGN.

6. DISCUSSION

6.1. *Comparison with Previous X-Ray Observations*

The data, normalized to the Crab Nebula, are listed in Table 1. Observations covering the same energy band should agree, but this is not the case. This *ROSAT* observation yields a count rate 3 times higher than the published *Einstein* IPC rate (Seward 1990). The IPC observation was short, only the bright center was visible, and the background assumed was high. These effects account for the discrepancy. At higher energies, $\sim$2–10 keV, the three scanning detectors give a rate 2–3 times higher than the two pointed detectors of *Einstein* and *EXOSAT*. Source confusion and background errors are the most plausible source of this discrepancy. It is also remotely possible that the AGN has a hard spectrum and is strongly variable. There is no evidence for this in the *ROSAT* observation, but the energy band here is small. CTA 1 has a softer spectrum than the Crab because of the soft thermal component and because the ISM column density is less.

6.2. *Cloudy ISM Model*

While the center-filled morphology of remnants such as CTA 1 differs from that expected from pure Sedov expansion into a uniform ISM, such a profile can result in a two-phase ISM consisting of discrete cool clouds surrounded by a uniform intercloud medium (White & Long 1991; hereafter WL). The scenario is as follows: upon explosion, a shock propagates quickly through the surrounding medium, leaving the cold clouds surrounded by hot postshock gas. These clouds slowly evaporate (Cowie & McKee 1977), increasing the density in the central regions of the remnant where initial temperatures are the highest. A similarity solution has been formulated for the evolution of a SNR in such a medium (WL), using the three standard Sedov parameters (the explosion energy E_0, the preshock ISM number density n_0, and the SNR age t) along with two new parameters: C, the ratio of ISM mass in clouds to that in the intercloud medium; and τ, the ratio of the cloud evaporation timescale to the SNR age.

The remnant age can be expressed as

$$t = 3.8 \times 10^2 R_{pc} (kT)_{keV}^{-1/2} \text{ yr} .$$

Thus, if the shock temperature can be determined, the SNR age can be derived directly from the measured radius. Assuming that the soft temperature component with $kT = 0.22$ keV is associated with the shock in CTA 1 yields a SNR age $t = 1.5 \times 10^4$ yr.

Using a numerical solution to the differential equations presented in WL, we have generated a series of models against which the observed radial profile of CTA 1 can be compared. The results after folding through N_H absorption and the PSPC efficiency are shown in Figure 6. It is important to note that, in addition to C and τ, the only input values for the model profiles are the X-ray luminosity, L_x, the shock temperature, T_s, the column density N_H, and the shock radius R_s, all of which are determined from the X-ray data. In order to accommodate extension from the bright central region of the remnant to the edges of the elongated structure, we assume a shock radius $R_s = 21.6$ pc, somewhat in excess of the 18 pc derived from the radio profile assuming spherical symmetry. We have also used a constant emissivity $\Lambda_x = 3 \times 10^{-22}$ cm^3 ergs s^{-1}, which is a reasonable approximation for a thermal plasma in equilibrium for the bandpass of the PSPC. It is clear from Figure 6 that appropriate combinations of C and τ can produce a surface brightness profile similar to that observed, although significant variations certainly exist.

Though we might expect some structure in the actual SNR profiles which would not be reproduced by the models, it is clear from Figure 6 that gross variations in the CTA 1 profiles extracted at different position angles around the remnant are not consistent with one another, thus causing this, and any radially symmetric model, to fail. The observed profile differences may be indicative of expansion into a medium with an overall density gradient (e.g., Chevalier 1982)—a scenario which could also result in a centrally bright morphology. Similarly, a change in column density across the remnant could produce a varying profile although we have not attempted to match the morphology by creating suitable N_H profiles. Alternatively, as discussed in § 6.3, it may be that the results are not the product of a simple blast-wave driven remnant into a complex medium. Lastly, as indicated in Table 6, the acceptable ranges of C and τ for the observed surface brightness profile implies a relatively weak explosion expanding into a very low density ISM. Direct determination of n_0 from the data is complicated because the spectral fitting was carried out only for discrete regions of the remnant in order to confine data to that from single pointings. As a result, the associated emitting regions are irregular in shape, and the volumes are difficult to estimate accurately. Rough estimates give $n_0 \sim 10^{-2}$ cm^{-3}. This value, which is reasonable for this region in the Galaxy, is considerably larger than those in Table 6.

TABLE 6

CLOUDY ISM SOLUTIONS FOR CTA 1 PARAMETERS

τ	C	n_0 (cm^{-3})	E_{51}	$M_x/M_\odot$
10.....	50	5.1×10^{-3}	0.083	40.8
30.....	150	4.2×10^{-3}	0.074	39.3
40.....	300	1.4×10^{-3}	0.059	35.7

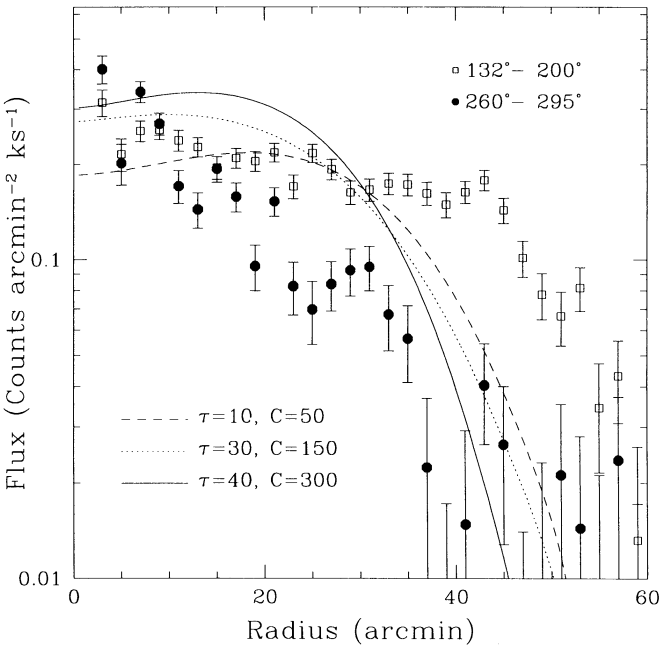

FIG. 6.—Model SNR radial profiles for evolution in cloudy ISM (after White & Long 1991; see text). Model parameters for upper and lower curves are indicated on plot. Calculations are based upon a shock temperature of 0.22 keV and absorption of log $N_H = 21.3$, as derived from spectral fits. Also shown are observed radial profiles for CTA 1 extracted from position angles between 132°–200° (*squares*) and 260°–295° (*circles*), where angles are measured counterclockwise from north.

We conclude that the cloudy ISM model can produce a center-filled morphology similar to that observed, but that considerable differences between the predicted and observed surface brightness profiles exist. The physical conditions implied by the model are somewhat extreme; the derived ISM density and SN explosion energy are very low. The model cannot be ruled out for CTA 1, but alternative interpretations may be equally plausible. One such alternative is that of a Sedov-type SNR with an embedded synchrotron source powered by a pulsar. We consider this in the next section.

6.3. *A Nonthermal Interior?*

Bearing in mind that evidence for radiation from the outer shell is secondary (the observed X-ray emission extends to the radio shell, the spectra require a soft component, and the relative contribution of this component is maximum at the limb), We can use the derived characteristics of this shell to calculate properties of the remnant. A simple blast wave model and formulae given by Rappaport et al. (1974) are used to derive age and energy release (see Table 7).

TABLE 7

BLAST WAVE CHARACTERISTICS

Parameter	Value
Distance used	1.4 kpc
Radius	18 ± 2 pc
Temperature	$0.23^{0.06}_{-0.02}$ keV
L_x (0.1–2.4 keV)	2.7×10^{34} ergs s^{-1}
Density of ISM, n_0	0.017 ± 0.003 atoms cm^{-3}
Age	$1.5 \pm 0.3 \times 10^4$ yr
Energy release, E_0	$2.8 \pm 0.4 \times 10^{49}$ ergs
Swept-up mass	$13 \pm 2\ M_\odot$

The derived ISM density, 0.017 atoms cm^{-3}, is low but not unreasonable if, at a distance of 1.4 kpc, CTA 1 is 250 pc above the Galactic plane. The amount of kinetic energy initially in the supernova debris, E_0, is 3×10^{49} ergs and is considerably lower than the 10^{51} ergs calculated for many other remnants. It is interesting to note that the energy of expansion of the Crab Nebula filaments is 1×10^{49} ergs (1 $M_\odot$ moving at 1000 km s^{-1}). If the Crab Nebula does not have an outer shell (which has so far eluded detection), this is E_0 for the Crab supernova.

Assuming that the "nonthermal" emission listed in Table 8 is synchrotron radiation, and that the radius of the synchrotron nebula is $\frac{1}{2}$ that of the blast wave, we can estimate the properties of the source. Assuming that the magnetic field, H, is uniform, that particles all have energy such that maximum emission is at 1 keV, and the nebular energy is equally divided between magnetic field and relativistic electrons, then we can derive magnetic field strength in terms of nebular size and luminosity (Seward 1983).

$$H(\mathrm{G}) = 25 L_x^{2/7}(\mathrm{ergs\ s^{-1}}) V^{-2/7}(\mathrm{cm^3})\ .$$

The result is $H = 3 \times 10^{-6}$ G and the lifetime of the X-ray emitting electrons is about the same as the age estimated for the shell, so this is a plausible situation.

If this nonthermal interpretation is correct, we might expect to find a pulsar associated with the central synchrotron nebula. Several pointlike sources are indeed found within the boundary of CTA 1. Source 7 is at the center of the nebula, the most likely position. A transverse velocity of 500 km s^{-1} would make sources 5 and 3 also candidates. A transverse velocity of 1200 km s^{-1} would be necessary for sources 4 and 6 at the southern edge of the central ridge. A search for pulsations from these sources was inconclusive, as expected, because we collected fewer than 50 counts from each source.

These data, then, are consistent with CTA 1 being an older Crab-like remnant. The argument for this is based on observations that the central region is the brightest part of the remnant and emits radiation with a hard spectrum. We note that the surface brightness of the synchrotron nebula is quite low, making detection in other wavebands difficult, as is the case for MSH 15–52 (Seward et al. 1984).

7. CONCLUSIONS

Using the *ROSAT* PSPC and HRI, we have investigated the spatial and spectral characteristics of CTA 1. We find a centrally peaked surface brightness with emission extending to the radio shell in the south and southeast, as well as into the radio-quiet region in the northwest. The X-ray spectrum requires both a soft and a hard component, although the data cannot differentiate between a two-temperature thermal model and a power-law/thermal model. The soft component dominates the outer regions of the remnant while the hard component dominates the center.

TABLE 8

SYNCHROTRON NEBULA CHARACTERISTICS

Parameter	Value
Distance	1.4 kpc
Assumed radius	9 pc
L_x (0.1–2.4 keV)	5.4×10^{34} ergs s^{-1}
Magnetic field strength, H	2.9×10^{-6} G
Magnetic field energy	3.2×10^{46} ergs
Electron lifetime	2×10^4 yr

Each model implies a specific interpretation for the SNR structure. Both scenarios appear quite plausible based upon the available data. For the thermal model, we have used the model of WL to generate surface brightness profiles for comparison with the observed profiles. We find that the observed physical characteristics, along with the parameters derived from the associated spectral fit, can reproduce the general features of the SNR surface brightness, but that details of the observed morphology differ considerably from the models. For this cloud evaporation scenario, the remnant must be the product of a somewhat weak explosion in a region of low density.

Alternatively, we have considered a central plerion interpretation for the morphology and hard central spectrum. This also requires an old remnant assuming that the soft component is associated with a Sedov-like shell. The central emission, if associated with a synchrotron nebula, implies a somewhat weak nebular magnetic field yielding a synchrotron lifetime for the X-ray–emitting electrons similar to the age of the remnant. A point source located within the centrally bright region of the remnant could be associated with the central pulsar required to power such a nebula.

Future observations with higher spectral resolution should clearly establish the thermal/nonthermal nature of the central regions.

This work was supported by the National Aeronautics and Space Administration through grant NAG5-1938 and contract NAS8-39073.

REFERENCES

Aschenbach, B. 1988, Appl. Opt., 17, 1404
Caraveo, P. A. 1993, ApJ, 415, L111
Chevalier, R. 1982, ApJ, 258, 790
Cowie, L. L., & McKee, C. F. 1977, ApJ, 211, 135
Fesen, R. A., Blair, W. P., Kirshner, R. P., Gull, T. R., & Parker, R. A. R. 1981, ApJ, 247, 148
Long, K. S., et al. 1991, ApJ, 373, 567
Maccacaro, T., Gioia, I. M., Stocke, J. T., Wolter, A., & Zamorani, G. 1988, ApJ, 326, 680
McHardy, I. M., et al. 1981, MNRAS, 197, 893
Ogelman, H. 1994, in The Lives of Neutron Stars, ed. A. Alpar, K. Kiziloglu, & J. van Paradijs (Dordrecht: Kluwer), in press
Pineault, S., Landecker, T. L., Madore, B., & Gaumont-Guay 1993, AJ, 105, 1060
Rappaport, S., Doxsey, R., Solinger, A., & Borken, R. 1974, ApJ, 194, 329
Rho, J.-H., Petre, R., Schlegel, E. M., & Hester, J. 1994, ApJ, 430, 757
Seward, F. 1983, in Supernova Remnants and their X-ray Emission, ed. J. Danziger & P. Gorenstein (Dordrecht: Reidel), 405
———. 1989, Space Sci. Rev., 49, 385
———. 1990, ApJS, 73, 781
Seward, F., Harnden, F. R., Jr., Swank, J., & Szymkowiak, A. 1984, ApJ, 281, 650
Seward, F., & Wang, Z-R. 1988, ApJ, 332, 199
Sieber, W., Haslam, C. G. T., & Salter, C. J. 1979, A&A, 74, 361
Sieber, W., Salter, C. J., & Mayer, C. J. 1981, A&A, 103, 393
Starke, A. A., Gammie, C. F., Wilson, R. W., Bally, J., Linke, R. A., Heiles, C., & Hurwitz, M. 1992, ApJS, 79, 77
Weiler, K. W. 1985, in The Crab Nebula and Related Supernova Remnants, ed. M. Kafatos & R. Henry (Cambridge: Cambridge Univ. Press), 265
White, R. L., & Long, K. S. 1991, ApJ, 373, 543 (WL)
Wood, K. S., et al. 1984, ApJS, 56, 507